Snihirova, D.; Lamaka, S.V.; Taheri, P.; Mol, J.M.V.; Montemor, M.F.:
Comparison of the synergistic effects of inhibitor mixtures tailored for enhanced corrosion protection of bare and coated AA2024-T3
In: Surface and Coatings Technology (2015) Elsevier

DOI: 10.1016/j.surfcoat.2015.10.075

Comparison of the synergistic effects of inhibitor mixtures tailored for enhanced corrosion protection of bare and coated AA2024-T3

D. Snihirova[a], S.V. Lamaka[a, b], P. Taheri[c], J.M.C. Mol[c], M.F. Montemor[a]

[a] Centro de Quimica Estrutural, Instituto Superior Técnico, Universidade de Lisboa, Av. Rovisco Pais, 1049-001 Lisboa, Portugal

[b] Magnesium Innovation Centre MagIC, Institute of Materials Research, Helmholtz-Zentrum Geesthacht, 21502, Germany

[c] Department of Materials Science and Engineering, Delft University of Technology, The Netherlands

Abstract

The replacement of chromate-based corrosion inhibitors is requirement for the aerospace sector. New developments demand additional studies to find synergistic combinations of inhibiting species. This paper discusses the synergistic effect resulting from various corrosion inhibitor mixtures proposed for corrosion protection of aluminum alloy AA2024-T3. Corrosion inhibition efficiency and the synergistic factors were determined for AA2024-T3 coupons immersed in 0.05 M NaCl solutions, containing either a single inhibitor or binary combinations of inhibitors. The following inhibitors were tested: Ce (III), 8-hydroxyquinoline (8HQ), salicylaldoxime (SAL), and 2,5-dimercapto-1,3,4-thiadiazolate (DMTD). Electrochemical impedance spectroscopy (EIS) and ATR-FTIR in Kretschmann geometry were used to evaluate the chemical and electrochemical variations during exposure of bare coupons to inhibitor-containing NaCl solutions. The results allowed for calculating the synergistic effect and the most effective mixtures were those containing 8HQ-SAL and DMTD-8HQ.

The synergistic effect was also determined for coated coupons. A water-based epoxy coating was modified with calcium carbonate microparticles, loaded beforehand with single inhibitors or with binary mixtures. EIS measurements were performed in 0.5 M NaCl and the results revealed that the epoxy coatings modified with $CaCO_3$ microparticles, loaded with inhibitor mixtures, provided enhanced corrosion protection. The most effective corrosion protection was observed for two mixtures: $CaCO_3$(8HQ+SAL) and $CaCO_3$(Ce+SAL). Interestingly, the results revealed that the synergistic effect on bare AA2024-T3 can be different from when the same inhibitor mixtures are used in smart, anti-corrosive coatings.

Keywords: synergistic mixtures, corrosion inhibitors, smart coatings, self-healing

1. Introduction

Several new concepts to design and manufacture smart materials have been developed over the last several years [1]. Among these, self-healing coatings are considered extremely promising for several applications, including corrosion protection of AA2024-T3. Self-healing coatings, modified with smart inhibitor carriers, are expected to provide long-term corrosion protection due to the controlled delivery of the active inhibiting species under specific, triggering conditions [2]. A crucial step in the design of such coatings is the choice of inhibitor. Presently, for aeronautic applications, chromates are still used in many steps, including pre-cleaning, conversion coating/anodizing, and as pigments. However, their high toxicity and environmental impact, has warranted intense research efforts to find environmental friendly alternatives. Finding appropriate replacement for the existing corrosion inhibitors, meeting the environmental and technical requirements, is still a major challenge [3, 4]. Recent works evidenced by combining two or more inhibitors improved corrosion inhibition to create a synergistic effect. Promising results were achieved by combining anodic and cathodic inhibitors [5-10]. Forsyth et al. [8] have studied the synergistic effect of cerium salicylate (CeSal) on mild steel. The improved performance of this combination of corrosion inhibitors, compared to each individually (i.e. Na(sal) and $CeCl_3$), was shown. Moreover, cerium dibutyl phosphate ($Ce(dbp)_3$) was tested as a substitute for chromates [5, 6]. Shi et. al [10] explored the inhibition efficiency of cerium cinnamate as an environmentally friendly additive in epoxy coatings. Recently, Kallip et al. [7] showed that there is a synergistic effect when combining anodic (1,2,3-benzotriazole) and cathodic ($Ce(NO_3)_3$) inhibitors on galvanically coupled Zn and Fe model cells. Yasakau et al. [11] studied the synergistic effect of cerium molybdate nanowires. Muster et al. [12] reported the optimization of mixtures of cathodic inhibitors (cerium, lanthanum and praseodymium), by applying a combinatorial design. It was predicted that the optimum inhibitor ratio in the mixture should be 72% cerium (Ce) and 28% (praseodymium (Pr)/lanthanum (La)) ions.

Mixtures of cerium, cobalt and manganese nitrates as corrosion inhibitors for AA 2024-T3 were studied by Balaskas et al. [9]. A synergistic effect between different inhibitors was not observed, but it was found that the best performing inhibitor, cerium nitrate, determined the overall anticorrosion performance.

The synergistic combination of corrosion inhibitors gives the idea of designing self-healing coatings. Once identified, it is possible to store these synergistic mixtures in "smart" containers which are, in turn, applied as additives to organic coatings [2]. This approach was followed up by Dias et al. [13]. The work reports an improvement of the corrosion protection of sol-gel coatings enhanced with a mixture of lanthanum and molybdate-enriched zeolite microparticles. The effect was attributed to synergistic protection, resulting from the release of the two distinct inhibitors from zeolites.

The present work aims to combine different, environmentally benign corrosion inhibitors and exploring the synergistic effect of binary inhibitor mixtures. Cerium cations (either Ce^{3+} or Ce^{4+}) have been reported as environmentally friendly inhibitors for oxygen reduction reactions and showing good inhibition efficiency on AA2024-T3 alloys [5, 12, 14-18]. The inhibiting mechanism of cerium cations is due to the blocking of the cathodic areas by oxide/hydroxide precipitates. Various organic inhibitors were also considered. 8-hydroxyquinoline [19-23] and salicylaldoxime [19, 24] have been reported as the most effective ones. They act as mixed-type corrosion inhibitors when used on AA2024-T3. The mechanism has been correlated to the formation of highly insoluble chelates, that suppress the dissolution of Mg, Al and Cu [19, 22]. Other candidates are copper complexants, such as 2,5-dimercapto-1,3,4-thiadiazolate (DMTD), which effectively stifles oxygen reduction on copper due to the formation of Cu-DMTD complexes which have limited aqueous solubility [25]. These organic compounds are generally less efficient than chromate, and their use is currently limited to corrosion protection of light airspace alloys [26].

In addition, this work aims at study the synergistic effects on coated samples that were modified with porous microparticles loaded with mixtures of corrosion inhibitor [27]. The binary mixtures Ce-DMTD, 8HQ-SAL, 8HQ-DMTD and Ce-SAL as well as seperately were selected for investigation in this work. In the first step the corrosion inhibition effect was studied on bare AA2024-T3 exposed to NaCl solutions. In the second step, the single inhibitors, or mixtures of these, were loaded into porous $CaCO_3$ particles, using a procedure described elsewhere [27]. These particles are pH sensitive and are expected to release the inhibitors when the pH at the anodic sites decreases [28].

2. Experimental

2.1 Materials

The following inhibitors were purchased from Aldrich: cerium(III) nitrate hexahydrate (Ref. 238538), 8-hydroxyquinoline (Ref. 252565), salicylaldoxime (Ref. 84172), 1,3,4-thiadiazole-2,5-dithiol dipotassium salt (Ref. 139432).

The AA2024-T3 coupons were chemically etched, using a three-step cleaning procedure as typically applied in the aeronautical industry. The AA2024-T3 coupons were cleaned in alkaline Metaclean T2001® at 60-70°C for 15-25 min, followed by alkaline etching in P3 Almeco 51® at 30-40°C for 3 min and acidic etching in TURCO Liquid Smutgo NC® at 30±5°C for 5-10 min. The coupons were briefly immersed (<1 min) in millipore water after each step, to remove the reaction products.

Calcium carbonate microbeads containing corrosion inhibitor were prepared according to the procedure reported by Snihirova et al [27]. The loading capacity of $CaCO_3$ for 8HQ, SAL and DMTD was measured using High-Performance Liquid Chromatography with a UV detector and were 0.97, 0.010 and 0.11 wt % respectively. The loading capacity of $CaCO_3$ for Ce^{3+}

was measured by Inductively Coupled Plasma Atomic Emission Spectroscopy and was 2.54 wt %. An epoxy model coating, without any pigments or anti-corrosion additives, a simplified primer formulation currently used in the aeronautical industry for the protection of AA2024-T3, was supplied by a coating manufacturer (the protected formulation is based on recent coating developments by the producer; thus, they cannot be disclosed here). The coating solution was loaded with a total concentration of 5 wt% (relative to the weight of the coating solution) of inhibitor-loaded $CaCO_3$ beads (Table 1).

System identification	Additives	
Epoxy	–	
Epoxy-$CaCO_3$(8HQ)	5wt%	$CaCO_3$ loaded with 8HQe
Epoxy-$CaCO_3$(SAL)	5wt%	$CaCO_3$ loaded with SAL
Epoxy-$CaCO_3$(DMTD)	5wt%	$CaCO_3$ loaded with DMTD
Epoxy-$CaCO_3$(Ce)	5wt%	$CaCO_3$ loaded with Ce
Epoxy-$CaCO_3$(Ce+SAL)	2.5wt%	$CaCO_3$ loaded with Ce
	2.5wt%	$CaCO_3$ loaded with SAL
Epoxy-$CaCO_3$(SAL+8HQ)	2.5wt%	$CaCO_3$ loaded with SAL
	2.5wt%	$CaCO_3$ loaded with 8HQ
Epoxy-$CaCO_3$(8HQ+DMTD)	2.5wt%	$CaCO_3$ loaded with 8HQ
	2.5wt%	$CaCO_3$ loaded with DMTD
Epoxy-$CaCO_3$(Ce+DMTD)	2.5wt%	$CaCO_3$ loaded with Ce
	2.5wt%	$CaCO_3$ loaded with DMTD

Table 1. List of prepared coating formulations.

The epoxy mixture loaded with $CaCO_3$ pH-sensitive particles was applied to the AA2024-T3 coupons by dip coating. The withdrawal rate was 18 cm/min and the immersion time in the coating solution was 100s. In order to obtain the required thickness, five consecutive dips

were performed. All coated coupons were cured at 50°C for 7h in air for further cross-linking and water evaporation.

2.2. Testing methods and equipment.

The interaction of the 8HQ, SAL and DMTD inhibitors with the aluminum surface was investigated by means of *in-situ* ATR-FTIR in Kretschmann geometry. Pure aluminum wire (99.95%), supplied by Goodfellow, were deposited on an internal reflection element hemisphere made of Ge (25 mm in diameter) from Harrick Scientific Products Inc. by means of a high-vacuum evaporation (Balzers BAE 250) coating system. The ATR-FTIR Kretschmann analyses were performed using a Thermo-Nicolet Nexus Fourier transform infrared spectroscopy (FTIR) apparatus, equipped with a mercury-cadmium-telluride liquid-nitrogen-cooled detector and a nitrogen-purged measurement chamber with a Harrick Seagull multipurpose reflection accessory. The measurements were performed with an incident beam angle of 65° using p-polarized radiation. For all FTIR analyses, the baseline spectra were recorded on untreated, deposited, aluminum layers, and the final measurements were recorded relative to the backgrounds.

To reveal the evolution of the microstructure of the surface, and changes in chemical composition of intermetallic particles during immersion tests, scanning electron microscopy (SEM/EDS) was employed. SEM images were taken with an FEG-SEM JEOL 7001 apparatus with an electron beam energy of 20kV.

The corrosion protection performance was assessed using electrochemical impedance spectroscopy (EIS). EIS measurements were performed using a Gamry FAS2 Femtostat, with a PCI4 Controller, in a frequency range from 100 kHz down to 10 mHz. The impedance spectra were taken at open circuit potential under a 10 mV sinusoidal perturbation. A conventional three-electrode electrochemical cell was used, consisting of a saturated calomel reference electrode, a platinum coiled wire as a counter electrode and the AA2024-T3

substrate as the working electrode. The area of the working electrode was approximately 3.14±0.2 cm^2. The electrochemical cell was placed inside a Faraday cage to avoid interferences from external electromagnetic fields and stray currents. EIS measurements were carried out on uncoated AA2024-T3 coupons immersed in an aqueous 1mM solution of inhibitor in 0.05 M NaCl. The protection efficiency of coated AA2024-T3 coupons was assessed during immersion in 0.5 M NaCl electrolyte. The total volume of electrolyte in the cell was 10 mL and it was quiescent as well as equilibrated with air. All measurements were performed at room temperature.

The inhibition efficiency (IE) values were calculated using the following equation:

$$IE = \frac{CR_0 - CR_{inh}}{CR_0} \quad (1)$$

were CR_0 is the corrosion rate in the non-inhibited medium, estimated as the inverse of charge transfer resistance (Rct), obtained by numerical fitting of the EIS data. CR_{inh} is the corrosion rate in the presence of $CaCO_3$/inhibitor in the coating.

Synergy occurs when the inhibitive effect of the mixture exceeds the sum of the individual components. The synergistic parameter (S) was calculated using equation (2) as proposed by Aramaki and Hackerman [29].

$$S = \frac{1 - IE_{1+2}}{1 - IE_{12}} \quad (2)$$

$$IE_{1+2} = (IE_1 + IE_2) - (IE_1 \times IE_2) \quad (3)$$

The parameters IE_1, IE_2 and IE_{1+2} are the inhibition efficiencies for inhibitors 1, 2 and the mixture of 1 and 2, respectively. IE_{12} is measured inhibition efficiency of the binary inhibitor mixture of 1 and 2. Synergistic effect S is the comparison of calculated value IE_{1+2} with the

measured one IE_{12}. Values of S > 1 indicate a synergistic effect of the selected inhibitor combination.

3. Results

3.1. Aluminum-inhibitor interface characterization by ATR-FTIR in Kretschman geometry

Investigation of the interfacial bonding of inhibitor molecules onto a pure aluminum surface, upon exposure to an aqueous solution containing inhibitor, was done by means of ATR-FTIR, in Kretschmann geometry [30]. In this measurement, a metallic film of nanometer thickness was deposited to an internal reflection element so that the IR radiation can pass through the metal layer and reach the metal-inhibitor interfaces. Figure 1 shows a schematic view of the set-up used for the near-surface analysis of the interface between an aluminum film and the corrosion inhibitor.

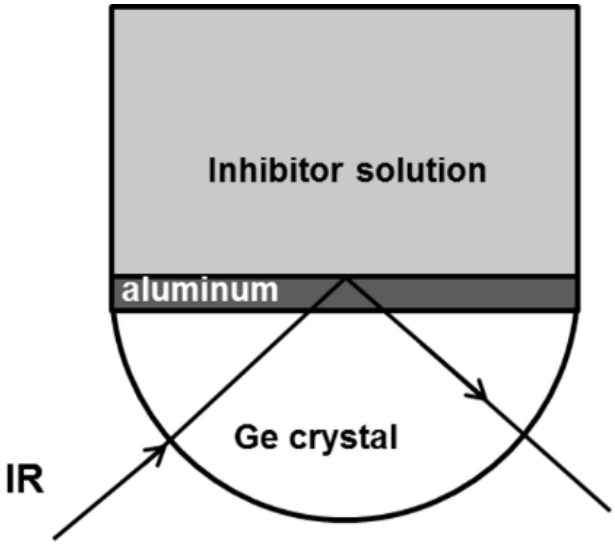

Figure 1 Schematic view of the ATR-FTIR experimental method based on Kretschmann geometry to analyze the interfacial interaction between aluminum surface and inhibitor.

Figure 2 presents the ATR-FTIR Kretschmann spectra of the Al layer after exposure to solutions containing 8HQ (a), SAL (b) and DMTD (c), after different immersion times. The spectra in Figure 2d were obtained after 30 min of immersion of internal reflection element (without aluminum layer) in electrolyte containing 8HQ and SAL. The spectra collected for

8HQ (a) show bands at 1410 cm^{-1} and 1460 cm^{-1} which can be associated with the stretching vibration of the aromatic C–C and C–N skeletal, respectively. The peaks around 1140 cm^{-1} can be attributed to the stretching vibration of C–O. The band around 2360 cm^{-1} represents the stretching and bending vibrations of C=O bond of absorbed CO_2 [31]. Figure 2a exhibits an intense negative band around 900 cm^{-1}, which increases with time. Figure 3b also shows a negative band at 885 cm^{-1} for the aluminum- salicylaldoxime system.

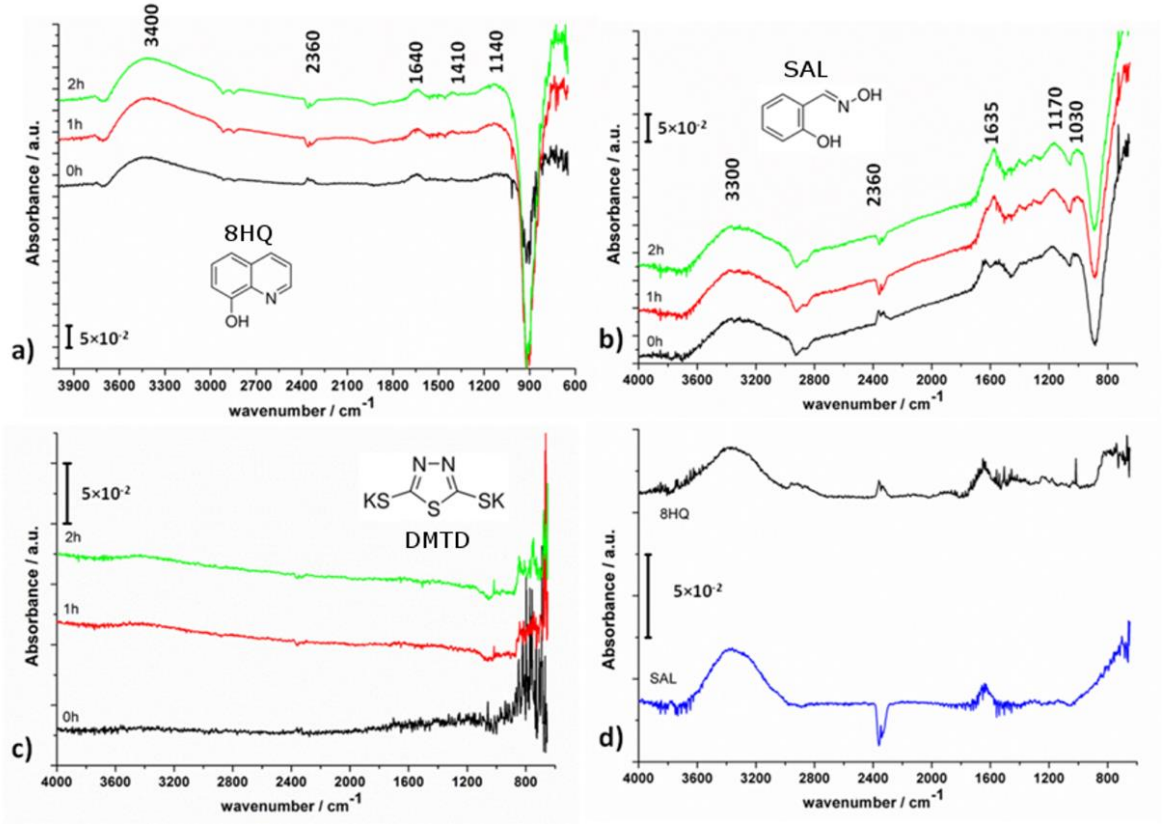

Figure 2. ATR-FTIR Kretschmann spectra of 8HQ (a), SAL (b) and DMTD (c) after 30s, 1h and 2h in contact with the Al layer and spectra of 8HQ and SAL (d) after 1h contact with surface of internal reflection element without aluminum on it.

The ATR-FTIR spectrum of DMTD (Figure 2c) did not show bands that would represent interaction between the inhibitor and Al surface. This result was expected since DMTD is known for its ability to form stable complexes with copper rather than aluminum [25, 32].

The evolution of adsorption depicted in Figure 3 shows the peak intensities at 921 and 885 cm $^{-1}$, corresponding to the fluorescent emission peak from the interaction of Al with 8HQ and SAL, respectively, versus the exposure time.

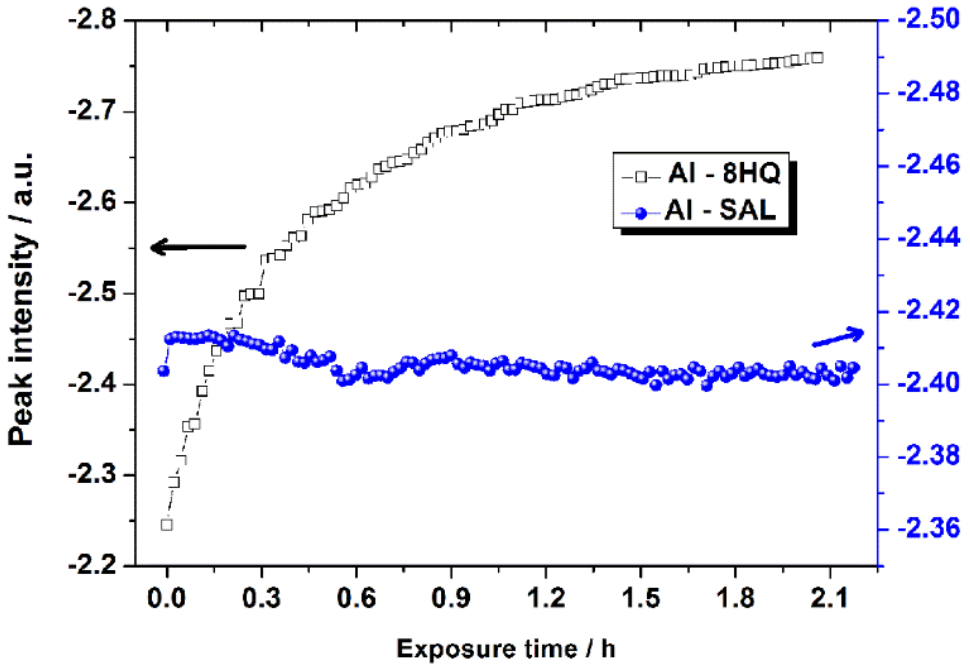

Figure 3. ATR-FTIR peak intensities of 8HQ and SAL at 920cm^{-1} and 885 cm^{-1} respectively versus the exposure time.

3.2. Microscopic characterization

SEM/EDS studies were performed for understanding the mechanism of corrosion inhibition by 2,5 –dimercapto- 1,3,4- thiadiazolate (DMTD) on AA2024-T3. The zones with different intermetallic (IM) particles were selected on a polished AA2024-T3 surface and all the IM particles were identified by EDS before immersion in the 1mM DMTD inhibitor solution (Figure 4a). The smaller round-shaped IM particles were identified as S-phase with an Al_2CuMg composition [33]. The second type of IM particles are those containing Fe, Mn, and Cu. The composition of the Fe-rich IM particles is shown in Figure 4b. A. Boag et al. [34] classified these particles in two groups based on the Si content and Cu/Fe ratio: $(Al,Cu)_x(Fe,Mn)_ySi$ and AlCuFeMn. The SEM image and the EDS elemental maps of Cu and

S were taken at exactly the same section of the alloy sample before, and after 30 min of, immersion in solution containing DMTD. The EDS elemental map on Figure 4c shows the location of the Cu-rich IM particles. The EDS map on Figure 4d shows the distribution of sulfur, the element constituting DMTD. The image indicates the presence of DMTD over the Cu-rich S-phase IM particles and its absence over Fe-rich IM particles.

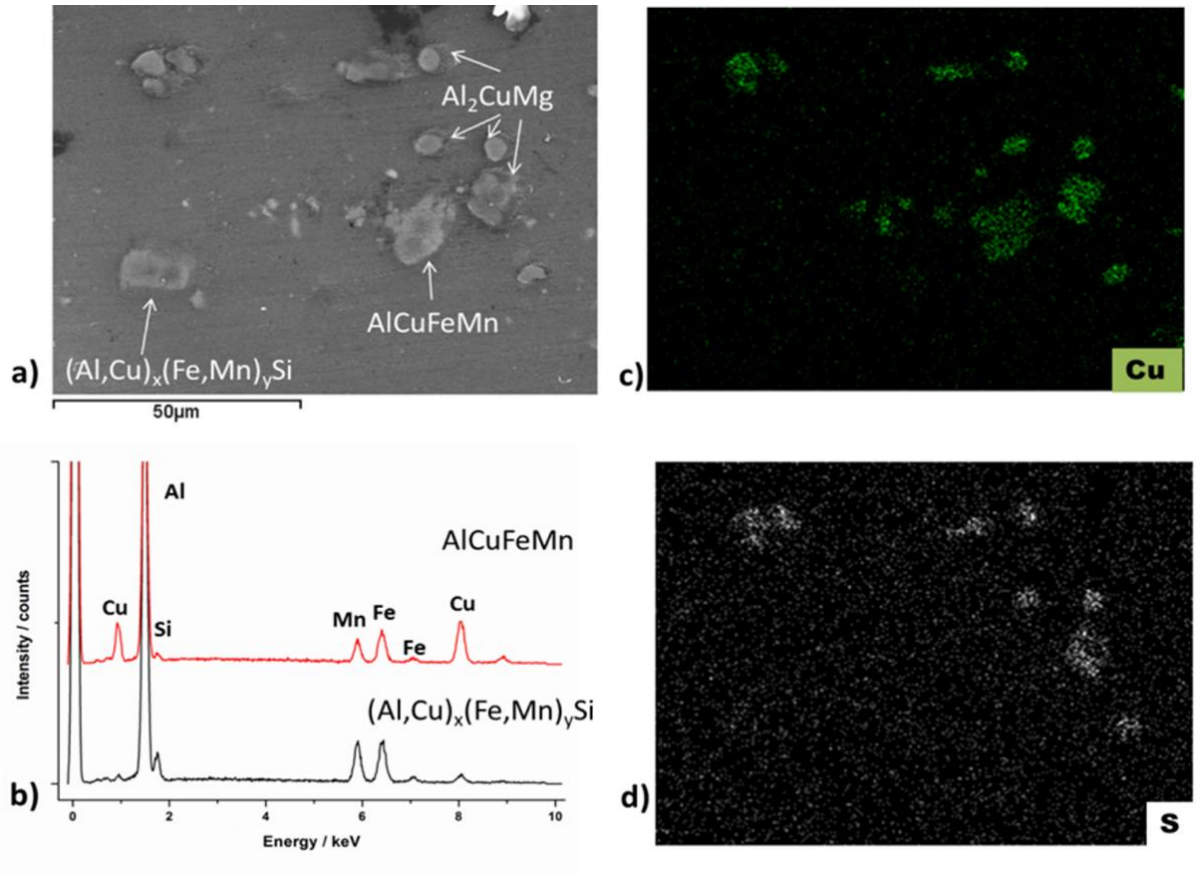

Figure 4. (a) SEM micrograph of IM particles after 30 min of exposure to 1mM DMTD solution.(b) X-ray spectra for corresponding IM on micrograph (a). The AlCuFeMn IM particles have a Cu/Fe ratio of 0.4 and 2.7 at.% Si whereas the $(Al,Cu)_x(Fe,Mn)_ySi$ IM particles have a Cu/Fe ratio of 2.5 and around 0.7 at.% Si. (c) and (d) images correspond to the EDS mapping of the area shown in (a).

The inhibition behavior of DMTD was also studied in a 0.1 M Cl^- ion solution. The EDS, elemental map in Figure 5c shows the location of Cu-rich IM particles. The signal of sulfur can be seen over the S-phase for the IM particles (Figure 5d) as was observed above. However, in contrast to a Cl^- free immersion, the presence of aggressive species promotes the interaction between DMTD and Fe-rich IM particles of the AlCuFeMn type.

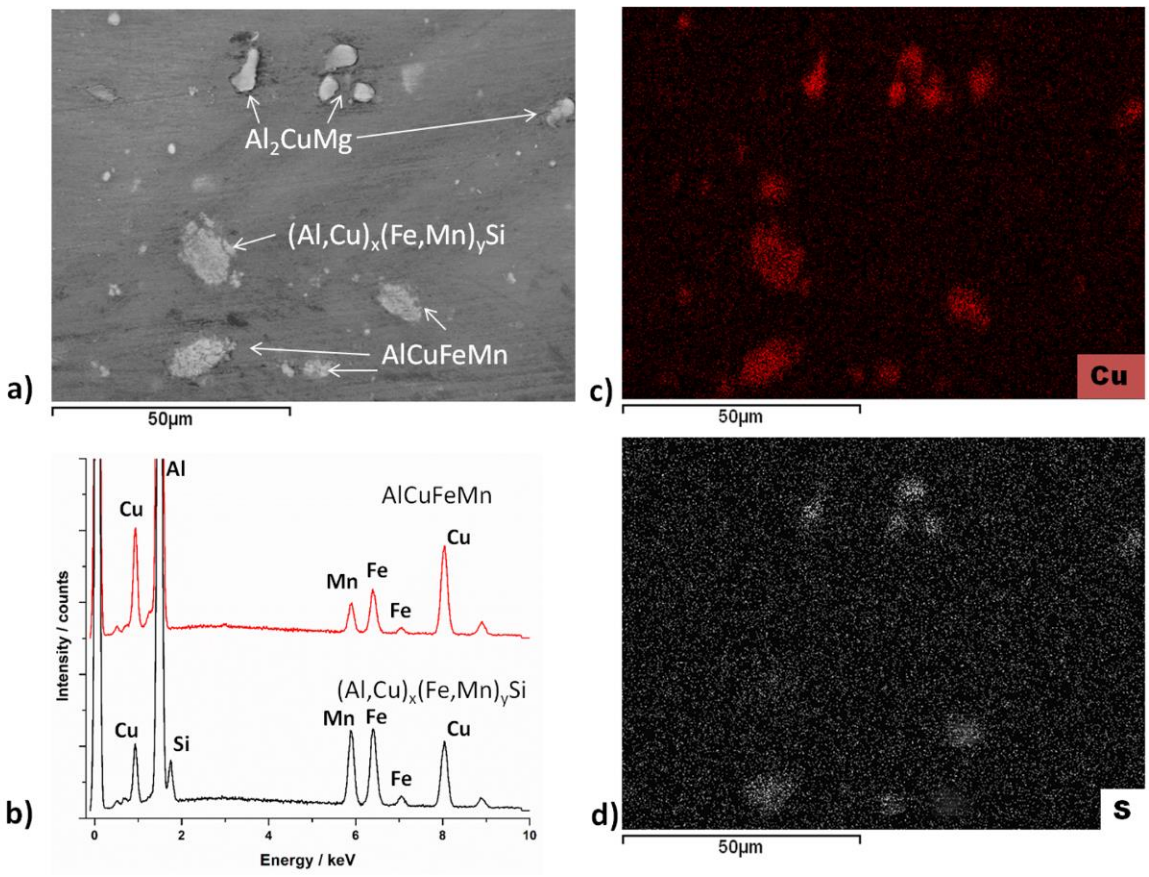

Figure 5. (a) SEM micrograph of IM particles after 30 min of exposure to 0.1 M NaCl with 1mM DMTD solution. (b) X-ray spectra for corresponding IM on micrograph (a). The AlCuFeMn IM particles have a Cu/Fe ratio of 0.4 and 2.7 at.% Si whereas the $(Al,Cu)_x(Fe,Mn)_ySi$ IM particles have a Cu/Fe ratio of 2.5 and around 0.7 at.% Si (c) and (d) images correspond to EDS mapping of the area shown in (a).

3.3. EIS investigation of anticorrosion properties of the inhibitors and their binary mixtures on bare AA2024-T3

The anticorrosion ability of single inhibitors and their mixtures was studied using electrochemical impedance spectroscopy (EIS) during immersion of bare coupons of AA2024-T3 in 1mM inhibitor plus 0.05 M NaCl electrolyte. For inhibitor mixtures, the total concentration of inhibitor was 1mM, consisting of 0.5mM of each inhibitor. The Bode plots obtained after 1 day of immersion are presented in Figure 6. The impedance spectra for bare AA2024-T3 reveals two time-constants. The medium frequency time constant can be assigned to the presence of a native oxide layer and the low frequency one is related to the corrosion process. The equivalent circuit depicted in Figure 6c was used to fit the experimental spectra for the alloy corroding in inhibitor free NaCl solution. Rel is the resistance of the electrolyte; Rox is the resistance of the native oxide layer; CPEox is the constant phase element representing the capacitance of the oxide film; Rct is the charge transfer resistance and CPEdl is constant phase element for the double layer capacitance.

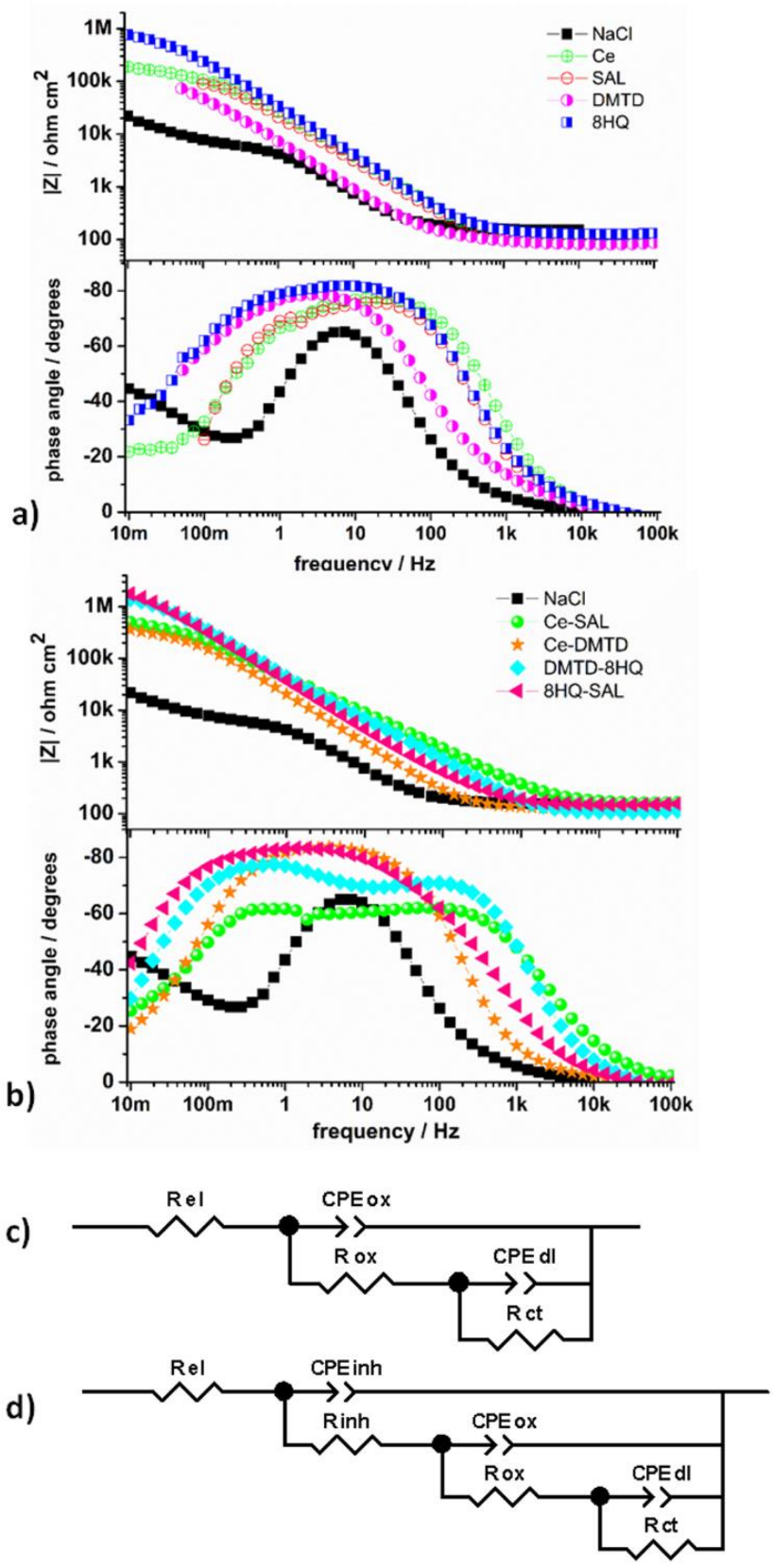

Figure 6. Electrochemical impedance Bode plots taken after 1 day of immersion of AA2024-T3 specimens in a) an inhibitor solution or b) in solution of inhibitor mixtures in 0.05 M NaCl; the equivalent circuit models used for fitting experimental spectra for c) AA2024-T3 immersed in 0.05 M NaCl and d) in inhibitor-containing NaCl electrolyte.

The impedance spectra for the AA2024-T3 immersed in the inhibitor containing electrolyte presents three time constants. The time constants at 1 Hz and 100 Hz are related to the native oxide film and the thin layer of inhibitor adsorbed on the surface respectively. The low frequency time constant can be assigned to the corrosion process. Figure 6d depicts the equivalent circuit used for fitting the impedance spectra obtained for AA2024-T3 immersed in the inhibitor-containing solution. The Rinh is the resistance of the inhibitor layer; CPEinh is constant phase element that characterizes the capacitance of the inhibitor film [19, 35]. The same model was applied for the inhibitor mixtures. For single inhibitors, the time constant related to the presence of an adsorbed layer was more defined with SAL and 8HQ. The same time constant evidences a wider phase angle for the samples immersed in DMTD and Ce, suggesting an overlap of both the medium and low frequency processes. Figure 7 presents the evolution of the native oxide layer resistance and the lowest values were observed for AA2024-T3 immersed in inhibitor-free NaCl solution. The addition of inhibitors leads to an increase of the oxide resistance by one or two orders of magnitude. The Rox decreases slightly for 8HQ, SAL and Ce but the values are still significantly higher than those observed in inhibitor-free solution.

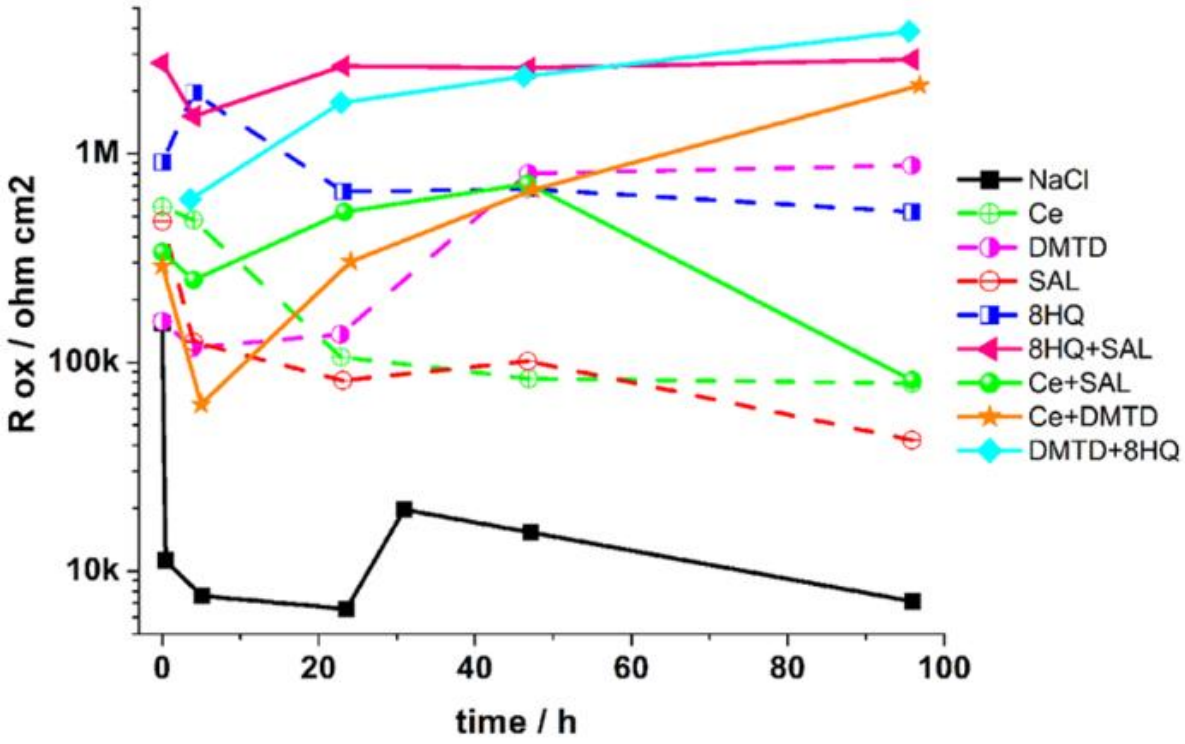

Figure 7 Evolution of oxide resistance during immersion in blank, or inhibitor-containing 0.05 M NaCl electrolyte.

3.4. Protective performance of epoxy coating with $CaCO_3$, doped with corrosion inhibitors or their mixtures

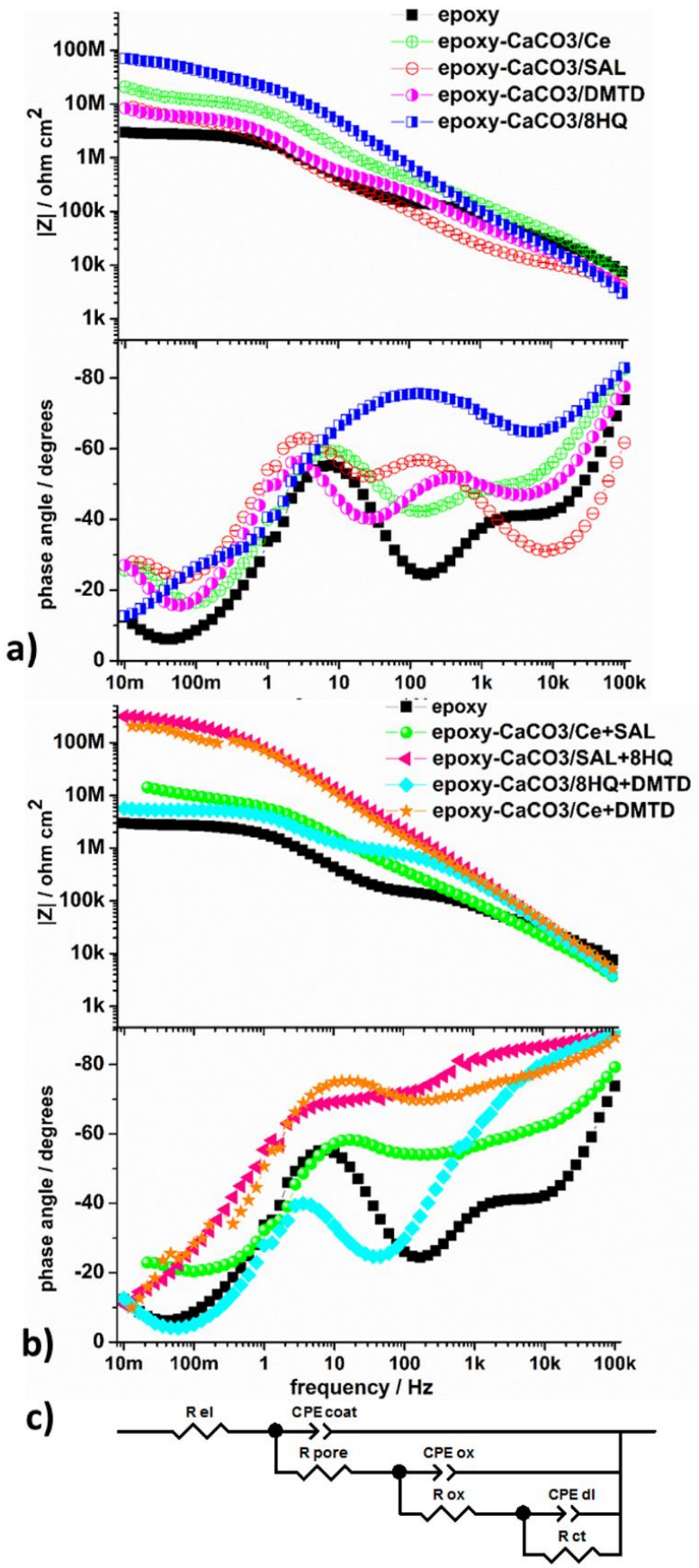

Figure 8. Electrochemical impedance Bode plots taken after 1 day of immersion of AA2024-T3 coated with epoxy, modified with a) $CaCO_3$ particles loaded with single inhibitors or b) $CaCO_3$ particles loaded with mixture of inhibitors and c) the equivalent circuit used for fitting experimental EIS data.

The "smart" protective properties of the epoxy coating with $CaCO_3$, loaded with single corrosion inhibitors were reported elsewhere [27]. In this work we used a similar epoxy coating but the average thickness of the coating was 13 µm, thinner than that reported in [27].

The corrosion resistance was assessed using EIS during immersion in 0.5 M NaCl. A set of representative plots is presented in Figure 8. The high frequency time constant, in the range 1kHz- 100kHz, reflects the evolution of the coating barrier properties. The time constant in the medium/low frequency range can be assigned to the intermediate aluminum native oxide layer, underneath the coating, whereas the one for the lowest frequencies is related to localized corrosion activity at the metallic substrate. The charge transfer resistance, extracted from the low frequency time constant, can be correlated with the effectiveness of the corrosion protection provided by the release of inhibitor stored from the microbeads.

All the coatings modified with $CaCO_3$ microparticles loaded with corrosion inhibitors reveal higher impedance values compared to the reference coating in the low frequency region. No signs of corrosion were found in the impedance spectra for the epoxy coatings loaded with 8HQ, 8HQ+SAL and Ce+DMTD after 1 week of immersion. The overall impedance of these coatings is above 70 $M\Omega\ cm^2$ after 1 week of immersion, highlighting the protective properties of the coating modified with $CaCO_3$ particles, in turn loaded with these inhibitors. Moreover, the results evidence that corrosion protection can be significantly improved by introducing mixtures of corrosion inhibitor. To estimate the charge transfer resistance and consequently the corrosion resistance, the impedance data was fitted with a combination of electrical elements configured into a set of equivalent circuits [27, 36, 37]. For the equivalent circuit depicted in Figure 8c, Rel accounts for the solution resistance; Rpore, Rox and Rct represent to the pore resistance of the coating, resistance of the intermediate oxide layer and

charge transfer resistance, respectively. CPEcoat, CPEox and CPEdl are the constant phase elements of the coating, oxide and double layer, respectively. Constant phase elements were used here instead of pure capacitances because of their deviations from an ideal capacitive behavior. The fitted Rpore and Rct values are depicted in Figure 9 as a function of time.

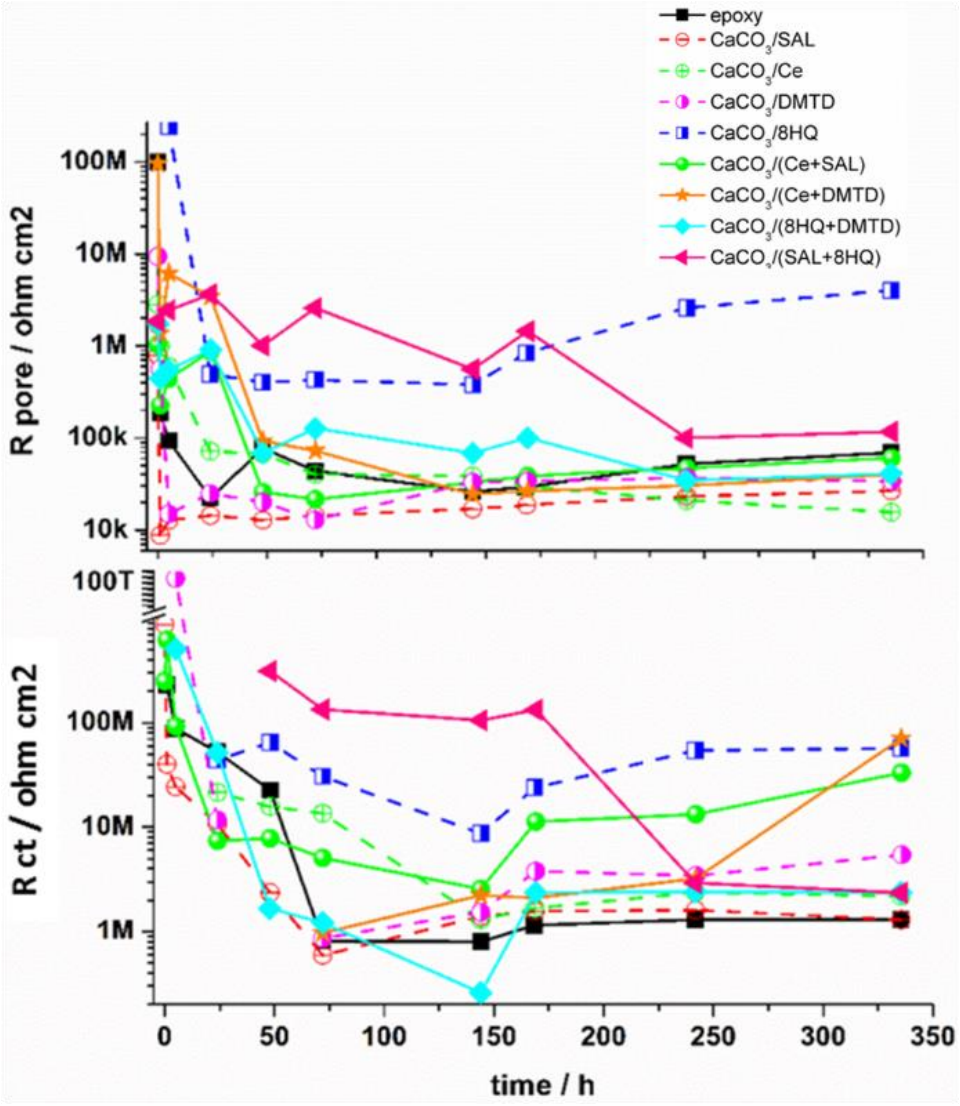

Figure 9 Evolution of the resistance parameters extracted by fitting for the highest frequency (Rpore) and low frequency (Rct) time constants, for the epoxy-coated AA2024-T3 samples immersed for 2 weeks in 0.5 M NaCl neutral solution.

The synergistic parameters S (calculated using eq. 2) are presented in Figure 10. This factor was above one for the mixture 8HQ+SAL during the first 7 days of immersion. This mixture demonstrates the highest synergistic effect (S=46.3) after 3 days of immersion. The result seems even more remarkable, when taking into account the two times lower concentration

(2.5 wt% $CaCO_3$/8HQ and 2.5 wt% $CaCO_3$/SAL) of each particular inhibitor in comparison with 5 wt% $CaCO_3$ for an individual inhibitor. These results are in agreement with EIS data obtained for bare AA2024-T3 exposed to NaCl and the mixture of 8HQ+SAL. For longer immersion time the synergistic effect decreases but remains above 1. After 1 week of immersion the cooperation effect becomes negligible. This fact can be associated with the lower loading capacity of organic inhibitors and faster release from the $CaCO_3$ particles distributed in the epoxy matrix [27].

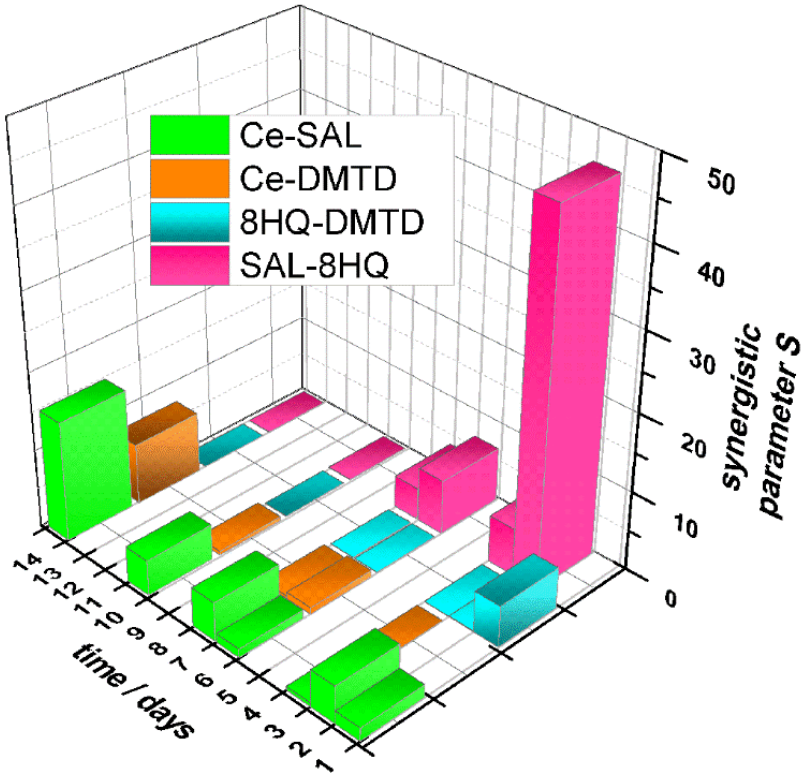

Figure 10. Evolution of synergistic parameter (S) for coated AA2024-T3 modified with $CaCO_3$ microparticles loaded with combinations of two inhibitors.

The mixture 8HQ+DMTD reveals S=5.3 after 2 days of immersion; for longer immersion time the enhanced effect was not observed. This effect can be explained by the decreased loading capacity for organic inhibitors and faster release from $CaCO_3$ in the epoxy matrix as explained above.

The inhibitive effect increases with time for the mixtures Ce+DMTD and Ce+SAL. After 2 weeks of immersion S= 7.8 for Ce-SAL and S=15.3 for Ce-DMTD were determined. It is worth noting that the system with Ce+SAL shows enhanced synergistic behavior for the entire 2 weeks. At early immersion stages, S was fluctuating but exhibiting values > 1. The highest value for S was observed after 2 weeks of immersion (S= 15.3).

4. Discussions

Characterization of the inhibitor-metal interaction

The corrosion protection effect and the mechanism of corrosion inhibition on bare AA2024-T3 were investigated using ATR-FTIR in Kretschmann geometry, SEM/EDS analysis and EIS. ATR-FTIR in Kretschmann geometry was performed in order to study inhibitor-aluminum interaction during immersion. Inhibitors SAL and 8HQ were found to be adsorbed on the surface of pure aluminum (Figure 2). The negative band with minima at 900 cm^{-1} for 8HQ and 885 cm^{-1} for SAL were assigned to fluorescence arising from the complex formed between the aluminum and inhibitor. The intensity of the band (Figure 2b) for SAL is lower compared to the negative band related to complex with 8HQ (Figure 2a) and probably due to larger π-conjugated system for 8-hydroxyquinoline which affects the fluorescence intensity [38]. Figure 2d present ATR-FTIR spectrum of SAL and 8HQ after 1h of contact with the surface of the internal reflection element without aluminum on it. The fluorescent-related bands for 8HQ and SAL were not observed indicating no interaction between the organic inhibitors and surface of the internal reflection element. Both inhibitors, 8HQ and SAL, have been reported to be cathodic inhibitors for aluminum and copper in neutral chloride solution [19, 21]. The inhibition mechanism is based on the formation of sparingly soluble complexes , in neutral media,with aluminum and copper. These adsorbates, confirmed by ATR-FTIR in Kretschmann geometry analysis, could be useable for the effective corrosion inhibition of AA2024-T3 because they can prevent the adsorption of chloride ions and destruction of the aluminum oxide layer. The peak intensity of the fluorescence related band for 8HQ increases

rapidly during the first hour of exposure due to an increase in inhibitor density as it is adsorbed on the surface (Figure 3). After exposure of more than 1.5 h, the intensity of the peak reaches a steady state, most probably due to saturation of the Al surface with 8HQ. The peak intensity of the fluorescent band of Al-SAL does not change with time. This means a fast adsorption of SAL on the aluminum surface. This is likely due to a higher number of functional groups (2 hydroxyl groups of SAL vs. 1 hydroxyl group of 8HQ), with which the inhibitor anchors itself to the metal surface, and less steric limitations for surface adsorption in comparison with 8HQ.

For the inhibitor DMTD no interaction was observed with bare aluminum (Figure 2c). These results were expected since the effectiveness of DMTD is limited to copper-rich intermetallics. As shown by Kendig et al. [39], DMTD effectively stifles oxygen reduction on copper due to the deactivation of Cu-rich IM particles and prevention of copper re-deposition. In order to investigate the interaction between DMTD and copper from intermetallic particles, an SEM/EDS analysis was conducted. DMTD was detected only on S-phase intermetallics after 30 min of immersion in a chloride free solution (Figure 4). The possible explanation for the selective reaction between DMTD and Cu from S-phase, can be as follows. The surface of AA2024-T3 is covered by a native oxide layer, which is thinner and contains more defects over the IM particles. Thus, more likely, corrosion attack occurs on the IM particles, especially over the S-phase, which have an electrochemical potential more negative than that of the Al matrix [40, 41]. Consequently, these particles behave anodically at the open circuit potential (OCP) and easily undergo dissolution. DMTD can interact with the Cu surface, forming low solubility chelates with copper ions. These chelates, which have limited solubility in water, precipitate selectively on the S-phase IM, inhibiting its dissolution. However, in the presence of Cl^-, precipitates of DMTD were also found on the AlCuFeMn (Figure 5) IM particles, probably due to the increased content of Cu in this intermetallic compared to $(Al,Cu)_x(Fe,Mn)_ySi$. In conclusion, DMTD interacts with Cu, with formation of

DMTD-derived precipitates or adsorbates on Cu-rich IM particles at the early stage of corrosion, and these species likely play a major role in the mechanism of inhibition [25, 32, 39].

EIS investigation of the anticorrosion properties of inhibitors.

Detailed analyses of the impedance spectra evolution obtained on bare AA2024-T3 immersed in inhibitor-containing 0.05 M NaCl solution shows that the presence of inhibitor mixtures confers an effective corrosion protection during the first day of immersion (Figure 6). Resistance of the oxide layer, extracted from the numerical modelling of the experimental data, was used to evaluate the inhibition efficiency. For longer term emersion of samples in solutions containing Ce and SAL, the Rox decreases but the values remained one order of magnitude above the reference sample. The behavior of the samples immersed in 8HQ-containing solution was distinct. Thus, there was a fast increase of Rox during the first day of immersion followed by a small decrease. The inhibition effect is due to the ability of 8HQ to form a dense and stable protective layer on the surface of AA2024-T3. This result is in good agreement with the ATR-FTIR results presented in Figure 3. The increase of the resistance of the oxide layer in the presence of DMTD reveals the positive effect of this inhibitor, especially in the longer term.

The analysis of the results depicted in Figure 7 suggests that the inhibition by 8HQ, SAL and DMTD is more effective than that by Ce. It is probably because of the effect of Ce^{3+} cations, which act as a cathodic inhibitor, and limited to the precipitation of hydroxides at the cathodic sites with elevated pH.

Most of the synergistic effect described in literature originated from mixing cathodic and anodic inhibitors [4-7, 9]. However, a synergistic effect may also be achieved by combining cathodic inhibitors as was shown by Muster et al. [12]. Galvanic corrosion of AA2024-T3 is a complex process, involving chemical and electrochemical processes including: dissolution of the S-phase, oxidation of Al and Mg, oxidation and redeposition of Cu, and reduction of

oxygen and water. Mixture of complexing agents as organic corrosion inhibitors may result in the strengthening of inhibition processes and synergistic effect. In this work, binary mixture of two cathodic inhibitors (Ce-DMTD), one cathodic and one mixed inhibitor (Ce-SAL, DMTD-8HQ) and two mixed-type inhibitors (8HQ-SAL), were studied. The beneficial inhibition activity of binary mixtures for short and long immersion times is presented in

. The samples immersed in the solutions containing the inhibitor mixtures DMTD-8HQ, 8HQ-SAL, Ce-DMTD showed the highest Rox and, therefore, the highest inhibition activity through long-term immersion. Note that compared to the other mixtures Ce-SAL performs well at the beginning of immersion but the corrosion activity increases after 2 days.

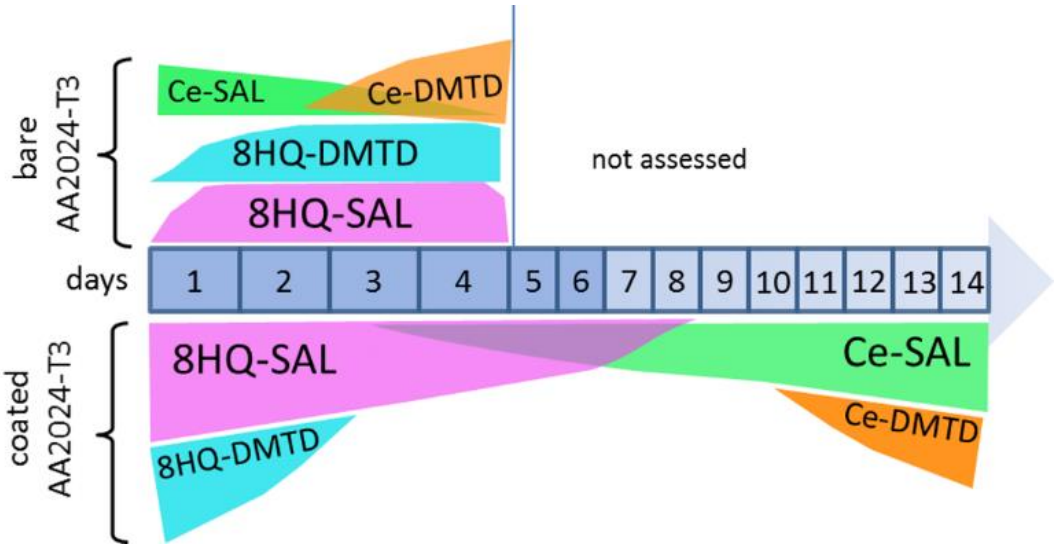

Figure 11 Time dependence of inhibition activity for binary mixtures on bare and coated AA2024-T3

A relevant question is if the efficiency and synergistic effects observed on uncoated parts exposed to the inhibitor solution can be extrapolated to a coated system. This is indeed a critical issue that has been scarcely discussed in recent literature. Thus, an identical study was performed for AA2024-T3 coated with a “smart” epoxy coating, i.e. with controlled inhibitor release. $CaCO_3$ microbeads were used for storage and pH-controlled release of the corrosion inhibitors.

Fitting results show that the addition of inhibitor-loaded $CaCO_3$ slightly decreases the barrier properties of the coating probably due to electrolyte uptake through the nanosized pores of the coating caused by the presence of $CaCO_3$ microbeads. Nonetheless, the protection offered by the inhibitors stored in the $CaCO_3$ is expected to compensate for the slight decrease of the epoxy barrier properties. On the other hand, addition of $CaCO_3$/8HQ, $CaCO_3$/(SAL+8HQ) and $CaCO_3$(8HQ+DMTD) increase the coating resistance. Interaction of a coating with an inhibitor is difficult to predict in advance, as it highly depends on the coating properties. For example 8HQ added directly to zirconium-based coating improves its barrier properties [42], while the same inhibitor embedded into an anodized layer and sealed with the same sol-gel coating leads to significant decomposition of the coating and deactivation of the inhibitor. This is most likely due to decomposition of relatively unstable and light-sensitive 8HQ on a porous, highly developed anodized surface [43]. The evolution of the low frequency resistance values, which is related to pitting activity shows that the selected inhibitors decrease the corrosion activity. The coatings modified with $CaCO_3$/DMTD, $CaCO_3$/SAL and $CaCO_3$/Ce display increased resistance at the early stages of immersion, but there is a decrease of the resistance with time.

Behavior of the Rct, extracted from the numerical fitting of experimental data, correlates with the effectiveness of the corrosion protection provided by the inhibitors. The evolution of Rct (Figure 9) shows that the Rct values increase for the system with $CaCO_3$/DMTD after 3 days of immersion. Thus, these inhibitors are most effective at the early stage. The results indicates that $CaCO_3$/8HQ reveals the most stable Rct values, which are one order of magnitude above that same parameter for the reference coating. The opposite effect was observed for bare metal, where Ce-SAL revealed improved protection at the beginning of immersion that then decreased significantly after 2 days of immersion.

summarizes the short and long term inhibition activity for bare AA2024-T3 and the substrate protected by “smart” epoxy coatings. CaCO3/(Ce-SAL) reveals the most effective inhibition

effect at longer immersion time. Binary mixture of cathodic inhibitors Ce-DMTD reveals enhanced inhibition at longer immersion time with synergistic effect S=7.8 after 2 weeks of immersion. This result was expected as the single inhibitors Ce and DMTD demonstrated corrosion protection at longer immersion. A delayed action of the Ce-DMTD mixture was also observed for bare coupons. The opposite effect was found for 8HQ-DMTD with the best corrosion protection at early stages of immersion for binary mixture and also each individual inhibitor. Further analyses shows that the most powerful inhibiting ability was conferred by $CaCO_3$/(SAL+8HQ). The calculated synergistic parameter in this case is significantly above 1 (S= 46.3) after 3 days of immersion. The same effect was observed for the bare metal. However, after 7 days of immersion, the inhibition ability in the coated samples decreased by 2 orders of magnitude. This fact can be attributed to the lower organic inhibitor loading capacity and faster release from $CaCO_3$ in an epoxy matrix [27]. It can be concluded that that binary mixtures 8HQ-SAL possess enhanced corrosion protection for both bare and coated AA2024-T3 for short immersion times only.

Based on the experimental evidence gathered, it can be concluded that corrosion protection ability of inhibitor mixtures cannot be simply predicted from in-solution inhibitor performance studies. The effect of inhibitors mixture on bare AA2024-T3 is different from that when the inhibitor mixtures are added to smart anti-corrosive coatings. Thus, successful tests in solution may not have the same result for coated parts.

5. Conclusions

ATR-FTIR Kretschmann spectroscopy indicated that 8HQ and SAL adsorb on Al surface forming a thin film, which provides a marked inhibition effect. No interaction of DMTD with pure Al was identified, while the results of SEM/EDS investigation showed that it forms precipitates or adsorbates on Cu-rich, intermetallic particles in AA2024-T3. Interaction of 8HQ and SAL with Al and DMTD with Cu play a major role in the mechanisms of corrosion inhibition.

The protection performance of inhibitors and their mixtures was assessed by electrochemical impedance spectroscopy. The inhibition effect was confirmed on bare and epoxy coated AA2024-T3. Epoxy coating modified with $CaCO_3$ microparticles loaded with individual inhibitors showed enhanced corrosion protection. This protection can be further improved owing to a synergistic effect between mixtures of two different inhibitors: Ce-SAL, Ce-DMTD, 8HQ-DMTD, SAL-8HQ. The highest synergistic effect for short immersion times was observed for mixtures SAL-8HQ, whereas for long immersion times the mixture Ce-SAL performs better.

This work demonstrates that corrosion protection ability of inhibitor mixtures cannot be simply predicted from in-solution inhibitor performance studies. The effect of inhibitor mixtures on bare AA2024-T3 is different from the behavior observed when inhibitor mixtures are added to smart anti-corrosive coatings. Thus, successful tests in solution may not have the same result for coated parts. This can be attributed to chemical interaction of released inhibitor with the components of the coating matrix. This interaction needs to be checked individually for each coating/inhibitor combination and coating/ mixture of inhibitors.

Acknowledgement

D. Snihirova would like to thank FCT for her PhD grant SFR/BD/72497/2010. D.Snihirova, S.Lamaka and F.Montemor also acknowledge CQE and FCT for the support through UID/QUI/00100/2013. S. V. Lamaka thanks the Alexander von Humboldt foundation for its financial support of her Experienced Researcher grant.

References

[1] K.A. Yasakau, J. Tedim, M.L. Zheludkevich, M.G.S. Ferreira, 10 - Smart self-healing coatings for corrosion protection of aluminium alloys, in: A.S.H. Makhlouf (Ed.) Handbook of Smart Coatings for Materials Protection, Woodhead Publishing2014, pp. 224-274.

[2] M.F. Montemor, Functional and smart coatings for corrosion protection: A review of recent advances, Surface and Coatings Technology, 258 (2014) 17-37.

[3] G. Bierwagen, R. Brown, D. Battocchi, S. Hayes, Active metal-based corrosion protective coating systems for aircraft requiring no-chromate pretreatment, Prog Org Coat, 68 (2010) 48-61.

[4] M.W. Kendig, R.G. Buchheit, Corrosion Inhibition of Aluminum and Aluminum Alloys by Soluble Chromates, Chromate Coatings, and Chromate-Free Coatings, Corrosion, 59 (2003) 379-400.

[5] J. Mardel, S.J. Garcia, P.A. Corrigan, T. Markley, A.E. Hughes, T.H. Muster, D. Lau, T.G. Harvey, A.M. Glenn, P.A. White, S.G. Hardin, C. Luo, X. Zhou, G.E. Thompson, J.M.C. Mol, The characterisation and performance of Ce(dbp)3-inhibited epoxy coatings, Prog Org Coat, 70 (2011) 91-101.

[6] N. Birbilis, R.G. Buchheit, D.L. Ho, M. Forsyth, Inhibition of AA2024-T3 on a Phase-by-Phase Basis Using an Environmentally Benign Inhibitor, Cerium Dibutyl Phosphate, Electrochemical and Solid-State Letters, 8 (2005) C180-C183.

[7] S. Kallip, A.C. Bastos, K.A. Yasakau, M.L. Zheludkevich, M.G.S. Ferreira, Synergistic corrosion inhibition on galvanically coupled metallic materials, Electrochem Commun, 20 (2012) 101-104.

[8] M. Forsyth, C.M. Forsyth, K. Wilson, T. Behrsing, G.B. Deacon, ATR characterisation of synergistic corrosion inhibition of mild steel surfaces by cerium salicylate, Corros Sci, 44 (2002) 2651-2656.

[9] A.C. Balaskas, M. Curioni, G.E. Thompson, Evaluation of Inhibitor Performance by Electrochemical Methods: Comparative Study of Nitrate Salts on AA 2024-T3, J Electrochem Soc, 161 (2014) C389-C394.

[10] H. Shi, E.-H. Han, S.V. Lamaka, M.L. Zheludkevich, F. Liu, M.G.S. Ferreira, Cerium cinnamate as an environmentally benign inhibitor pigment for epoxy coatings on AA 2024-T3, Prog Org Coat, 77 (2014) 765-773.

[11] K.A. Yasakau, J. Tedim, M.F. Montemor, A.N. Salak, M.L. Zheludkevich, M.G.S. Ferreira, Mechanisms of Localized Corrosion Inhibition of AA2024 by Cerium Molybdate Nanowires, The Journal of Physical Chemistry C, 117 (2013) 5811-5823.

[12] T.H. Muster, H. Sullivan, D. Lau, D.L.J. Alexander, N. Sherman, S.J. Garcia, T.G. Harvey, T.A. Markley, A.E. Hughes, P.A. Corrigan, A.M. Glenn, P.A. White, S.G. Hardin, J. Mardel, J.M.C. Mol, A combinatorial matrix of rare earth chloride mixtures as corrosion inhibitors of AA2024-T3: Optimisation using potentiodynamic polarisation and EIS, Electrochim Acta, 67 (2012) 95-103.

[13] S.A.S. Dias, S.V. Lamaka, T.C. Diamantino, M.G.S. Ferreira, Synergistic Protection against Corrosion of AA2024-T3 by Sol-Gel Coating Modified with La and Mo-Enriched Zeolites, J Electrochem Soc, 161 (2014) C215-C222.

[14] K.A. Yasakau, M.L. Zheludkevich, S.V. Lamaka, M.G.S. Ferreira, Mechanism of corrosion inhibition of AA2024 by rare-earth compounds, Journal of Physical Chemistry B, 110 (2006) 5515-5528.

[15] L. Paussa, F. Andreatta, N.C. Rosero Navarro, A. Durán, L. Fedrizzi, Study of the effect of cerium nitrate on AA2024-T3 by means of electrochemical micro-cell technique, Electrochim Acta, 70 (2012) 25-33.

[16] A.J. Aldykewicz, H.S. Isaacs, A.J. Davenport, The Investigation of Cerium as a Cathodic Inhibitor for Aluminum-Copper Alloys, J Electrochem Soc, 142 (1995) 3342-3350.

[17] A.M. Homborg, E.P.M. van Westing, T. Tinga, G.M. Ferrari, X. Zhang, J.H.W. de Wit, J.M.C. Mol, Application of transient analysis using Hilbert spectra of electrochemical noise to the identification of corrosion inhibition, Electrochim Acta, 116 (2014) 355-365.

[18] T.H. Muster, D. Lau, H. Wrubel, N. Sherman, A.E. Hughes, T.G. Harvey, T. Markley, D.L.J. Alexander, P.A. Corrigan, P.A. White, S.G. Hardin, M.A. Glenn, J. Mardel, S.J. Garcia, J.M.C. Mol, An investigation of rare earth chloride mixtures: combinatorial optimisation for AA2024-t3 corrosion inhibition, Surface and Interface Analysis, 42 (2010) 170-174.

[19] S.V. Lamaka, M.L. Zheludkevich, K.A. Yasakau, M.F. Montemor, M.G.S. Ferreira, High effective organic corrosion inhibitors for 2024 aluminium alloy, Electrochim Acta, 52 (2007) 7231-7247.

[20] D. Snihirova, S.V. Lamaka, M.M. Cardoso, J.A.D. Condeço, H.E.C.S. Ferreira, M. de Fatima Montemor, pH-sensitive polymeric particles with increased inhibitor-loading capacity as smart additives for corrosion protective coatings for AA2024, Electrochim Acta, 145 (2014) 123-131.

[21] G.P. Cicileo, B.M. Rosales, F.E. Varela, J.R. Vilche, Inhibitory action of 8-HYDROXYQUINOLINE on the copper corrosion process, Corros Sci, 40 (1998) 1915-1926.

[22] S.-m. Li, H.-r. Zhang, J.-h. Liu, Corrosion behavior of aluminum alloy 2024-T3 by 8-hydroxy-quinoline and its derivative in 3.5% chloride solution, Transactions of Nonferrous Metals Society of China, 17 (2007) 318-325.

[23] K.A. Yasakau, M.L. Zheludkevich, O.V. Karavai, M.G.S. Ferreira, Influence of inhibitor addition on the corrosion protection performance of sol–gel coatings on AA2024, Prog Org Coat, 63 (2008) 352-361.

[24] G.P. Cicileo, B.M. Rosales, F.e. Varela, J.R. Vilche, Comparative study of organic inhibitors of coppercorrosion, Corros Sci, 41 (1999) 1359-1375.

[25] G. Williams, A.J. Coleman, H.N. McMurray, Inhibition of Aluminium Alloy AA2024-T3 pitting corrosion by copper complexing compounds, Electrochim Acta, 55 (2010) 5947-5958.

[26] S.R. Taylor, B.D. Chambers, Identification and Characterization of Nonchromate Corrosion Inhibitor Synergies Using High-Throughput Methods, Corrosion, 64 (2008) 255-270.

[27] D. Snihirova, S.V. Lamaka, M.F. Montemor, “SMART” protective ability of water based epoxy coatings loaded with CaCO3 microbeads impregnated with corrosion inhibitors applied on AA2024 substrates, Electrochim Acta, 83 (2012) 439-447.

[28] D. Snihirova, S.V. Lamaka, M. Taryba, A.N. Salak, S. Kallip, M.L. Zheludkevich, M.G.S. Ferreira, M.F. Montemor, Hydroxyapatite Microparticles as Feedback-Active Reservoirs of Corrosion Inhibitors, ACS Appl Mater Interfaces, 2 (2010) 3011-3022.

[29] K. Aramaki, N. Hackerman, Inhibition Mechanism of Medium-Sized Polymethyleneimine, J Electrochem Soc, 116 (1969) 568-574.

[30] M. Öhman, D. Persson, ATR-FTIR Kretschmann spectroscopy for interfacial studies of a hidden aluminum surface coated with a silane film and epoxy I. Characterization by IRRAS and ATR-FTIR, Surface and Interface Analysis, 44 (2012) 133-143.

[31] P. Taheri, J.R. Flores, F. Hannour, J.H.W. de Wit, H. Terryn, J.M.C. Mol, In Situ Study of Buried Interfacial Bonding Mechanisms of Carboxylic Polymers on Zn Surfaces, The Journal of Physical Chemistry C, 117 (2013) 3374-3382.

[32] L. Huang, F. Tang, B.X. Hu, J. Shen, T. Yu, Q.J. Meng, Chemical reactions of 2,5-dimercapto-1,3,4-thiadiazole (DMTD) with metallic copper, silver, and mercury, Journal of Physical Chemistry B, 105 (2001) 7984-7989.

[33] R.G. Buchheit, R.P. Grant, P.F. Hlava, B. McKenzie, G.L. Zender, Local Dissolution Phenomena Associated with S Phase (Al[sub 2]CuMg) Particles in Aluminum Alloy 2024-T3, J Electrochem Soc, 144 (1997) 2621-2628.

[34] A. Boag, A.E. Hughes, A.M. Glenn, T.H. Muster, D. McCulloch, Corrosion of AA2024-T3 Part I: Localised corrosion of isolated IM particles, Corros Sci, 53 (2011) 17-26.

[35] M.L. Zheludkevich, K.A. Yasakau, S.K. Poznyak, M.G.S. Ferreira, Triazole and thiazole derivatives as corrosion inhibitors for AA2024 aluminium alloy, Corros Sci, 47 (2005) 3368-3383.

[36] M.L. Zheludkevich, R. Serra, M.F. Montemor, K.A. Yasakau, I.M.M. Salvado, M.G.S. Ferreira, Nanostructured sol–gel coatings doped with cerium nitrate as pre-treatments for AA2024-T3: Corrosion protection performance, Electrochim Acta, 51 (2005) 208-217.

[37] S.V. Lamaka, M.L. Zheludkevich, K.A. Yasakau, R. Serra, S.K. Poznyak, M.G.S. Ferreira, Nanoporous titania interlayer as reservoir of corrosion inhibitors for coatings with self-healing ability, Prog Org Coat, 58 (2007) 127-135.

[38] Y. He, C. Zhong, A. He, Y. Zhou, H. Zhang, Synthesis and luminescent properties of novel bisfunctional polymeric complexes based on carbazole and 8-hydroxyquinoline groups, Mater. Chem. Phys., 114 (2009) 261-266.

[39] M. Kendig, C. Yan, Critical concentrations for selected oxygen reduction reaction inhibitors, J Electrochem Soc, 151 (2004) B679-B682.

[40] A. Boag, R.J. Taylor, T.H. Muster, N. Goodman, D. McCulloch, C. Ryan, B. Rout, D. Jamieson, A.E. Hughes, Stable pit formation on AA2024-T3 in a NaCl environment, Corros Sci, 52 (2010) 90-103.

[41] N. Birbilis, M.K. Cavanaugh, L. Kovarik, R.G. Buchheit, Nano-scale dissolution phenomena in Al–Cu–Mg alloys, Electrochem Commun, 10 (2008) 32-37.

[42] A.F. Galio, S.V. Lamaka, M.L. Zheludkevich, L.F.P. Dick, I.L. Müller, M.G.S. Ferreira, Inhibitor-doped sol–gel coatings for corrosion protection of magnesium alloy AZ31, Surface and Coatings Technology, 204 (2010) 1479-1486.

[43] S.V. Lamaka, G. Knörnschild, D.V. Snihirova, M.G. Taryba, M.L. Zheludkevich, M.G.S. Ferreira, Complex anticorrosion coating for ZK30 magnesium alloy, Electrochim Acta, 55 (2009) 131-141.